RESEARCH ARTICLE

Special Section:
An Appraisal of Global Continental Crust: Structure and Evolution

Key Points:
- We present the first detailed study of crustal structure at Lake Tanganyika using receiver functions inversion and forward modeling
- Crustal thinning along the eastern Tanganyika rift basin is ~20% but may increase beneath the central basin
- Elevated V_P/V_S ratios, evidence for gradational Moho, and deep seismicity suggest previously unrecognized role of magma intrusion

Supporting Information:
- Supporting Information S1

Correspondence to:
F. Illsley-Kemp,
f.illsley-kemp@soton.ac.uk

Crustal Structure at a Young Continental Rift: A Receiver Function Study From the Tanganyika Rift

Isabel Hodgson[1], Finnigan Illsley-Kemp[1] (iD), Ryan J. Gallacher[1,2], Derek Keir[1,3] (iD), Cynthia J. Ebinger[2] (iD), and Khalfan Mtelela[4]

[1]Ocean and Earth Science, National Oceanography Centre Southampton, University of Southampton, Southampton, UK, [2]Department of Earth and Environmental Sciences, Tulane University of Louisiana, New Orleans, LA, USA, [3]Dipartimento di Scienze della Terra, Università degli Studi di Firenze, Florence, Italy, [4]Department of Geology, University of Dar es Salaam, Dar es Salaam, Tanzania

Abstract The southern Tanganyika Rift, within the Western rift, Africa, has earthquakes to depths of 37 km, yet few constraints exist on crustal thickness, or of early stage rifting processes in apparently amagmatic rift sectors. The aim of the TANGA14 experiment was to constrain bulk crustal properties to test whether magmatic processes modify the lithosphere in areas of deep seismicity, and the degree of lithospheric thinning. We use 11 broadband seismometers to implement receiver function analysis using H-κ stacking, a method sensitive to crustal thickness and V_P/V_S ratio, to determine bulk crustal properties. Analyses include extensive error analysis through bootstrap, variance, and phase-weighted stacking. Results show the Archean Tanzanian Craton and Bangweulu Block are characterized by V_P/V_S ratios of 1.75–1.77, implying a felsic bulk composition. Crust beneath the fault-bounded basins has high V_P/V_S ($>$1.9). Anorthosite bodies and surface sediments within the region may contribute to localized high V_P/V_S. However, elevated V_P/V_S values within fault-bounded extensional basins where elevated heat flow, hydrothermal vent sites, and deep earthquakes are observed suggest that magma may be intruding the lower crust beneath the southern Tanganyika Rift. Crustal thicknesses on/near the relatively unextended Tanzanian craton and Bangweulu Block are 41.6–42.0 km. This contrasts with the Tanganyika Rift where crustal thicknesses are 31.6 km to 39 km from north to south. Our results provide evidence for ~20% crustal thinning localized to fault-bounded basins. Taken together, they suggest a previously unrecognized role of magma intrusion in early stage continental rifting in the Western rift, Africa.

1. Introduction

Numerical models predict that tectonic forces are insufficient to initiate rifting of thick, strong continental lithosphere and favor magmatic processes for helping to initiate extension of the East African rift system (EARS) (Bialas et al., 2010; Buck, 2004; Koptev et al., 2015). The EARS lies above a large-scale mantle low-velocity zone interpreted as one or more mantle plumes (e.g., Debayle et al., 2001; Ebinger & Sleep, 1998; Hansen & Nyblade, 2013; Halldórsson et al., 2014). Yet magmatism in the Western rift is volumetrically small and spatially restricted to isolated volcanic complexes such as the Katwe-Kikorongo, Virunga, S. Kivu, and Rungwe volcanic provinces (Ebinger, 1989; Halldórsson et al., 2014) (Figure 1). Regional surface wave studies of the Rukwa-Malawi region show mantle low-velocity zones localized to the Rungwe volcanic province (Accardo et al., 2017). Using *Pn* and *Sn* phases from sparsely distributed seismic stations along other sectors of the Western rift, tomographic models of O'Donnell et al. (2014) reveal seismic velocities indicative of normal mantle temperature. The spatial scale of localized magmatic processes, however, may be less than the resolving power of these tomographic methods.

The Western rift system is characterized by unusually long (80–120 km) border faults, broad uplifted flanks, and broad basins containing ~7 km of sedimentary strata (e.g., Morley, 1988; Morley et al., 1992; Rosendahl et al., 1986). Rift morphology and long faults can be explained by stretching of strong, cold continental lithosphere (e.g., Ebinger et al., 1991). Frequent earthquakes at depths of 25–40 km in the Tanganyika Rift have been interpreted as evidence for strong, cold crust and upper mantle, although earlier interpretations were limited owing to the lack of information on the depth to the crust-mantle boundary (Craig et al., 2011; Foster & Jackson, 1998; Yang & Chen, 2010).

In order to address the current inconsistency between observations that lack evidence for magmatic activity, and models which suggest tectonic forces are not sufficient to initiate rifting, we use receiver function
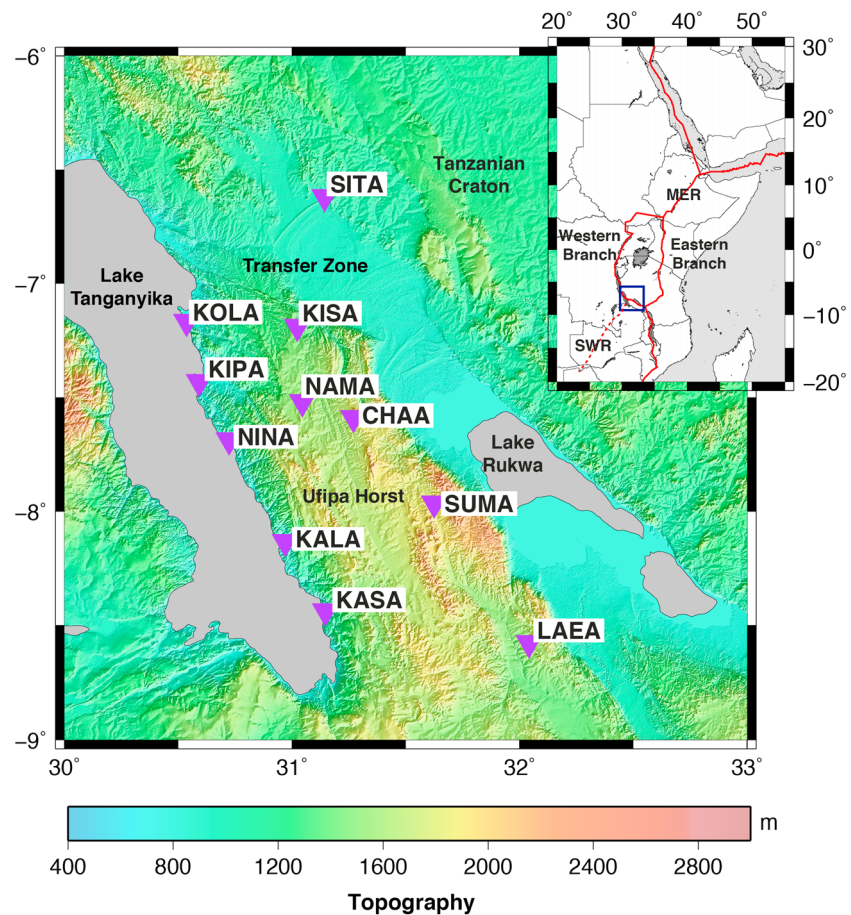
Figure 1. Map of Lake Tanganyika and surrounding region showing the distribution of stations (purple inverted triangles) and the fault-bounded area of low topography that previously connected the Tanganyika and Rukwa lake basins. The WNW striking oblique-slip fault system is referred to as the Tanganyika-Rukwa Transfer Zone (TRTZ). Inset: the East African Rift with the Eastern and Western branches bounding the Tanzanian Craton, the Main Ethiopian Rift (MER), the Southwestern Rift (SWR) and the study area outlined in blue.

analysis from the first dense network of seismic stations deployed on the southern Tanganyika Rift section of the EARS in Tanzania. We image crustal thickness and bulk crustal V_P/V_S, the ratio of the compressional wave velocity to the shear wave velocity of a seismic ray. This enables us to test the hypothesis of whether magmatic intrusion and/or partial melt are present within the crust. Bulk crustal composition has been successfully used to evaluate the presence of magmatism in other regions such as the Cameroon Volcanic Line (Gallacher & Bastow, 2012), the Main Ethiopian Rift (MER) (Cornwell et al., 2010), and the Eastern rift in Tanzania and Kenya (Plasman et al., 2017).

By performing a receiver function analysis of bulk crustal seismic structure, the crustal thickness (H) and V_P/V_S ratio (κ) of the Tanganyika Rift are obtained. The identification of bulk V_P/V_S values gives an insight into the bulk composition of the crust at a given location. While it is difficult to constrain percent partial melt and percent solidified mafic intrusion versus continental crust with seismological techniques (Hammond & Kendall, 2016), it is expected that magmatic modification of the crust would result in bulk V_P/V_S values greater than around 1.8 (Christensen, 1996). Insight into the crustal thickness variation should improve our understanding of deep earthquakes in continental rift zones, and the manifestation of continental crust extension between the two rift segments Tanganyika and Rukwa.

2. Background

Faults bounding the Tanganyika Rift transect three major geological terrains: the Tanzanian Craton, the Bangweulu Block, and a series of Proterozoic belts bounding each craton (Figure 2). The Tanzanian Craton
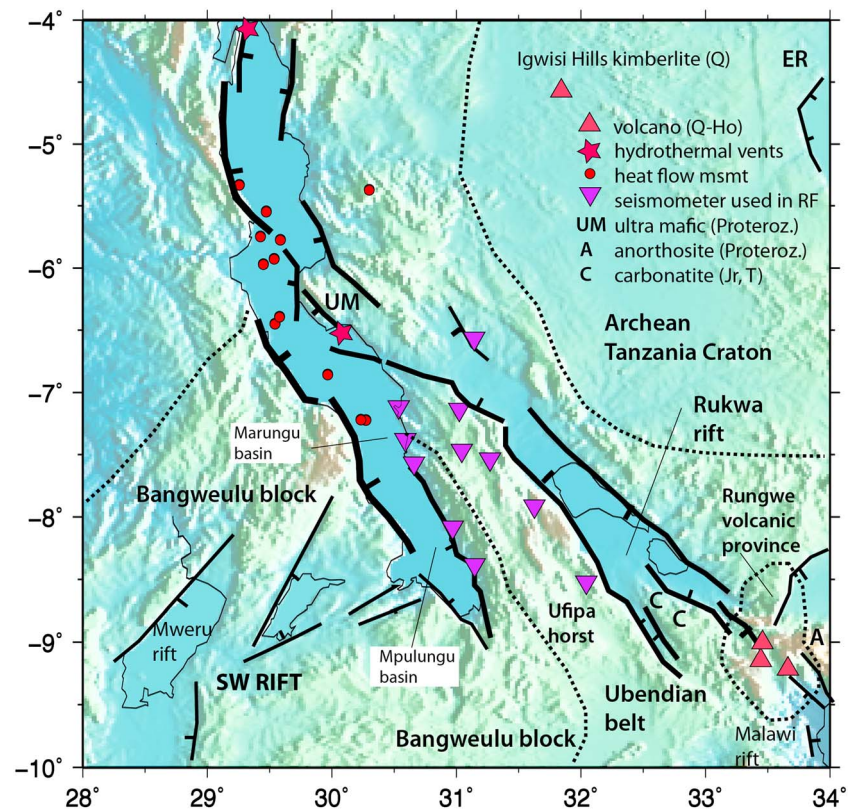
Figure 2. Tectonic map of the region of interest (Coussement et al., 1994; Ebinger et al., 2013; Lenoir et al., 1994). Eastern Rift (ER), Southwestern Rift (SW Rift), Holocene (Ho), and Quaternary (Q).

comprises Archean terrains that coalesced ~2.6 Ga (Bellucci et al., 2011 and references therein) which can be characterized by very low surface heat flow (~34 mW/m^2) (Nyblade et al., 1990). The Tanzanian Craton has deep buoyant roots, enabling stability over several Ga (Bellucci et al., 2011, and references therein). The Bangweulu block also appears to be deeply rooted from regional surface and body wave tomography studies (Fishwick & Bastow, 2011; Mulibo & Nyblade, 2013).

The Tanzanian Craton and Bangweulu Block were linked by several Proterozoic belts in the Precambrian (e.g., Lenoir et al., 1994; McConnell, 1950) (Figure 2). The Ubendian belt was accreted laterally onto the Tanzanian Craton during the collision between the Tanzanian Craton and Bangweulu Block (Lenoir et al., 1994) during the African orogeny 2.1–2 Ga. Since the Paleoproterozoic the NW-SE trending structures of the Ubendian belt have experienced periods of reactivation along sheared structures (Lenoir et al., 1994). The belt hosts gneiss layers which dip steeply at terrane boundaries. The most prevalent lithology within the belt is amphibole-bearing orthogneiss (diorite to granite) with rare quartzites and metacalcareous rocks hosting remnants of high *P-T* rock associations (Lenoir et al., 1994).

The Tanganyika Rift hosts 80–100 km long, NW striking, large-offset, normal faults creating broad asymmetric rift basins containing up to 7 km fluviolacustrine sedimentary rocks (Ebinger, 1989; Morley, 1988; Rosendahl, 1987). The border faults accommodate most of the strain across the basins, based on balanced reconstructions and flexural models (e.g., Ebinger et al., 1991; Morley, 1988; Morley et al., 1992). Along the length of the rift, strain is transferred via time-varying transfer fault zones that are oblique to the opening direction (e.g., Morley, 1988; Rosendahl et al., 1986). Using seismic reflection data, Morley (1988) showed that the amount of crustal extension locally decreased along single basins toward the transfer zones, providing evidence that transfer zones include en echelon and sometimes overlapping, extensional faults that form locally broader zones of extension.

The southern Tanganyika rift study area comprises from north to south parts of the Moba, Karema, Marungu, and Mpulungu border faults and corresponding half-graben basins (Ebinger, 1989; Morley, 1988). The

Tanganyika-Rukwa Transfer Zone (TRTZ) is a WNW striking oblique-slip fault zone linking strain in the Tanganyika rift to the subparallel Rukwa rift to the east (Ebinger, 1989; Morley, 1988) (Figures 1 and 2).

There are few constraints on the age of Western rift initiation, with estimates of ~12 Ma from projection of modern depositional rates (Cohen et al., 1993; Scholz et al., 2011). Volcanic provinces to the north and south of the rift initiated at 12 Ma and 17 Ma (e.g., Kampunzu et al., 1998), although U-Pb dates of carbonatitic tuffs in the Rukwa area dated at ~25 Ma, suggesting parts of the Western rift may be older (Roberts et al., 2010). Roberts et al. (2012) argue synchronous rifting of the Western and Eastern rifts can be attributed to extensional stresses caused by widespread plume uplift derived from either singular or multiple plume source(s).

The order of magnitude difference in volume of erupted volcanic products between the Western and Eastern rifts is linked to the presumed location of one or more mantle upwelling(s) on the eastern side of the deeply keeled Tanzanian craton, which blocks the flow of hot plume material susceptible to adiabatic decompression melting (e.g., Ebinger & Sleep, 1998; Koptev et al., 2015; Weerarante et al., 2003). This negates the requirement for multiple plumes and is consistent with geochemistry assigning a single mantle source for both branches either side of the craton (Chakrabarti et al., 2009; Halldórsson et al., 2014).

Although no Tertiary eruptive volcanic products have been mapped along the length of the Tanganyika Rift, Coussement et al. (1994) identified hydrothermal sites with sulfides in Lake Tanganyika, suggesting magmatic contributions (Tiercelin et al., 1989). These hydrothermal sites may be surface expressions of deep-seated magma chambers below fault junctions at the base of the crust which may also be responsible for elevated heat flow measurements (e.g., Ebinger, 1989; Nyblade et al., 1990).

Little is known of upper mantle structure beneath the Western rift, in large part owing to the lack of data from the Democratic Republic of the Congo (DRC), which borders the western side of the rift. Global and regional arrays provide some background. O'Donnell et al. (2015) use Pn and Sn tomography to image variations in uppermost mantle velocity associated with heating and magmatism. They find little evidence for reduced Pn or Sn velocities beneath southern Lake Tanganyika and argue against magmatic modification. Body wave tomography from temporary arrays in East Africa reveals low velocities beneath the southern Tanganyika and Rukwa Rift zones, with the largest velocity anomalies beneath the Miocene-Recent Rungwe volcanic province (Accardo et al., 2017; Mulibo & Nyblade, 2013). Surface and body wave tomography models of East Africa indicate that lithospheric thickness is ≥200 km beneath the Congo and Tanzania cratons, and between 100 and 200 km beneath the Western rift zone (Craig et al., 2011; Fishwick & Bastow, 2011). Lithospheric thinning, therefore, could be as much as 30%. Elastic plate thickness (Te) derived from coherence analysis of topography and Bouguer anomaly (Pérez-Gussinyé et al., 2009) and forward modeling of gravity and topography (Ebinger et al., 1991) shows reduction of Te to 15–30 km within the fault-bounded basins. The continental scale crustal model for Africa derived by modeling the free-air gravity anomaly developed from Gravity Recovery and Climate Experiment data (Tedla et al., 2011) predicts crust in the region of the Tanganyika rift to be between ~35 and 40 km.

Using the evidence for a lack of significant magmatism in the western rift, O'Donnell et al. (2015) suggest that a combination of gravitational stresses, combined with dynamic feedbacks between faulting, topography, and weathering could add to tectonic stresses and facilitate rifting (e.g., Stamps et al., 2015). Alternatively, mantle buoyancy forces and tractions facilitate rifting (e.g., Sembroni et al., 2016). Receiver function analyses of widely spaced stations along the Western rift show little difference in crustal structure between the Archean craton and Proterozoic belt, suggesting that crustal structure has had little influence on the location of rifting (Tugume et al., 2012). Our study utilizes a denser network of seismometers within the rift and across the broad uplifted flanks. The array has sufficient spatial resolution to image crustal thinning and any magmatic modification within the Ufipa horst between the Tanganyika and Rukwa rift (Figure 2).

3. Method

Thirteen broadband seismometers were deployed on the southeastern shore of Lake Tanganyika (Figure 1) for 15 months from June 2014. Eleven stations of the network were used, and 457 teleseismic earthquakes were recorded. Teleseismic earthquakes with magnitudes ≥6.5 were filtered between 0.04 Hz and 3 Hz using a Butterworth filter. Manual quality control based on a high signal-to-noise ratio and spectral energy with no
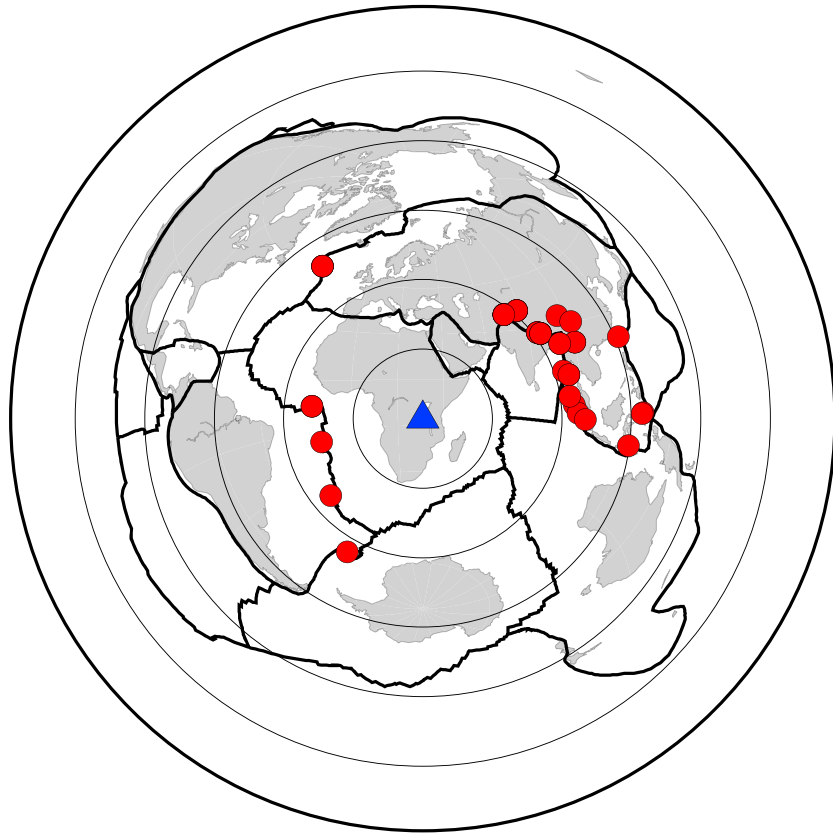
Figure 3. The global distribution of all the teleseismic events used to produce receiver functions following quality control plotted with an azimuthal equidistant map projection. Concentric circles indicate 30° intervals from the center.

high mode energy interference was performed and the epicentral distance restricted to between 30° and 95°. After the quality control, 40 very high quality events were selected for receiver function analysis (Figure 3).

A teleseismic body wave consists of an initial P wave followed by a coda made up of mode-converted energy; the result of the impedance contrasts at the Moho (Phinney, 1964). If we approximate the crust as a single horizontal layer, deconvolving the vertical component of the teleseismic arrival from the radial component yields a receiver function. This receiver function contains the initial P wave arrival, followed by phase arrivals that represent four phase conversions (Figure 4). The assumption of a single crustal layer can lead to anomalous results, as a complex Moho can cause additional phase arrivals (e.g., Hayes & Furlong, 2007). The
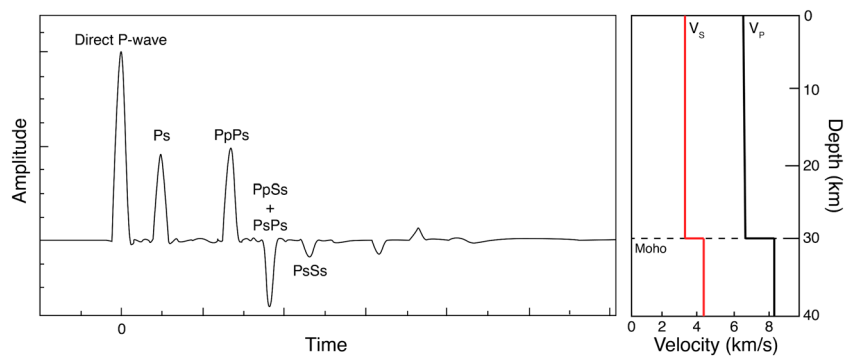

Figure 4. (left) An idealized receiver function produced using a (right) velocity model with the reverberation phase arrivals labeled. Upgoing incident waves and downgoing reflected crustal waves are denoted by uppercase letters; upgoing converted waves are denoted by lowercase letters. In practice, the receiver function contains much more noise, effectively hiding the PsSs phase. By stacking the data, the signal-to-noise ratio is increased.

deconvolution of the vertical component is a mathematically unstable procedure; this study uses the Extended-Time Multitaper Frequency Domain Cross-Correlation Receiver Function method of Helffrich (2006). This method develops upon earlier spectral analysis work by Park and Levin (2000) and Thomson (1982).

We completed quality control of the computed receiver functions by observing the noise present prior to the P wave arrival and then use the H-κ stacking method of Zhu and Kanamori (2000). This provides crustal thickness results (H) and bulk crustal V_P/V_S ratios (κ) by using the following equations:

$$t_{Ps} = H\left(\sqrt{\frac{1}{V_s^2 - p^2}} - \sqrt{\frac{1}{V_p^2 - p^2}}\right),$$ (1)

$$t_{PpPs} = H\left(\sqrt{\frac{1}{V_s^2 - p^2}} + \sqrt{\frac{1}{V_p^2 - p^2}}\right),$$ (2)

$$t_{PpSs+PsPs} = H\left(2\sqrt{\frac{1}{V_s^2 - p^2}}\right),$$ (3)

where t_X is the arrival time of each respective phase and p is the ray parameter of the teleseism. Zhu and Kanamori (2000) found that the arrival times of the distinct phases are not sensitive to changes in P wave velocity such that a 0.1 km s^{-1} change in V_P leads to <0.5 km uncertainty in crustal thickness. Therefore, a global continental crustal average V_P of 6.6 km s^{-1} is assumed for the crust (Christensen & Mooney, 1995) due to the lack of local constraints for the study region. As the incident angle of the incoming teleseism is ~90° the phase arrival times are less affected by lateral variations in the crust; thus the receiver function can be approximated as a point measurement (Zhu & Kanamori, 2000). A grid search is applied across the reverberation arrival times until they are coherently stacked. A crustal thickness and V_P/V_S range of 20 km to 50 km and 1.6 to 2.2 were used through the grid search stack as these were deemed the most geologically reasonable values.

One of the main advantages of this stacking method is that the arrival times of each phase conversion do not need to be manually picked: consequently, vast amounts of teleseismic data can be processed efficiently. By calculating the theoretical arrival time for each phase conversion and plotting these on the receiver functions, quality control of the data can be undertaken and the accuracy of the results is improved. Furthermore, by using teleseismic events with a wide range of azimuths and distances the effects of proximal lateral structures are minimized.

4. Error Analysis

Error analysis of the data establishes the accuracy and reliability of the obtained results. A combination of error analysis techniques, outlined below, were implemented to ascertain whether our results were robust. As outlined in the discussion, the error analysis conducted herein is more comprehensive than reported in earlier studies by Tugume et al. (2012), and offers insight into differences between results.

The 95% confidence interval (Figure 5a) is a gauge for the accuracy of the H-κ analysis. In addition, Zhu and Kanamori (2000) use the Taylor expansion of s(H,κ) at the maximum and omit the higher-order terms to determine the variances ($\sigma_{H/\kappa}^2$) of H and κ:

$$\sigma_H^2 = 2\sigma_s / \frac{\partial^2 s}{\partial H^2}$$ (4)

$$\sigma_\kappa^2 = 2\sigma_s / \frac{\partial^2 s}{\partial \kappa^2}$$ (5)

where σ_s is the standard error of the stack at the maximum. However, Eaton et al. (2006), found this method unsuitable as the error of H and κ tends to increase with the number of receiver functions used in a stack. This is counterintuitive, as one would expect accuracy to increase when more data are stacked. Furthermore, the error derived from equations (4) and (5) produced symmetrical ellipses which do not denote the trade-off
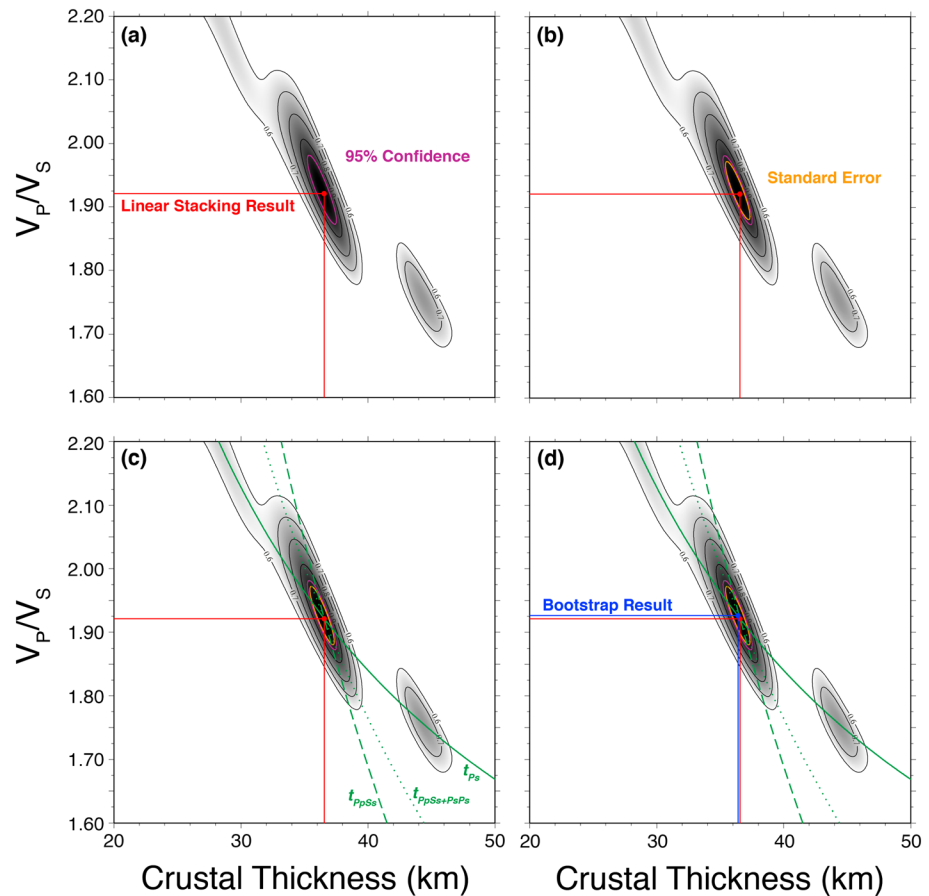
Figure 5. Examples of synthetic H-κ stacks with the linear stacking result (red point). Shown are error analysis techniques: (a) 95% confidence (purple contour); (b) standard error contour (orange contour); (c) H and κ values derived from t_{Ps} (solid green), t_{PpPs} (dashed green), and $t_{PpSs + PsPs}$ (dotted green) arrivals; and (d) the bootstrap result (blue point).

between H and κ values indicated by the inclined elongated contours of the stacking function. To remedy these problems Eaton et al. (2006) suggest estimating uncertainties in H and κ by plotting contours in the stack that are one standard error below the maximum value and represent the variance of the stack, this is given as $\left(\sigma_s^2/N\right)^{0.5}$. We plot the standard error as a contour below the maximum (Figure 5b). Once the H and κ values have been obtained, the phase arrivals t_{Ps}, t_{PpPs}, and $t_{PpSs + PsPs}$ (calculated using equations (1)–(3)) can be used to visually inspect the dependence of the stack on each phase (Zhu & Kanamori, 2000) (Figure 5c).

We also use the phase-weighted stacking method to provide a further measure of the robustness of our results (Schimmel & Paulssen, 1997; Thurber et al., 2014). This method assists in the detection of weak, coherent signals typical of lower mantle P-to-S conversions and removes incoherent noise from the receiver functions. Each receiver function is assigned a stack weighting dependent on the receiver function coherency with respect to other receiver functions for a station. The phase stack varies between 0 and 1 as a function of time and is calculated by

$$c(t) = \frac{1}{N}\left|\sum_{j=1}^{N} e^{\left[i\phi_j(t)\right]}\right|, \tag{6}$$

where N is the number of receiver functions used and $\Phi j(t)$ is the instantaneous phase of the jth receiver function. The instantaneous phase is obtained by separating phase and amplitude information using a Hilbert transform and allows the comparison of receiver functions based on phase rather than amplitude (Schimmel & Paulssen, 1997). If the phases of a receiver function are incoherent $c(t)$ will equal 0 and the receiver function will be discarded from the stack. However, if the phases are coherent and $c(t)$ equals 1,
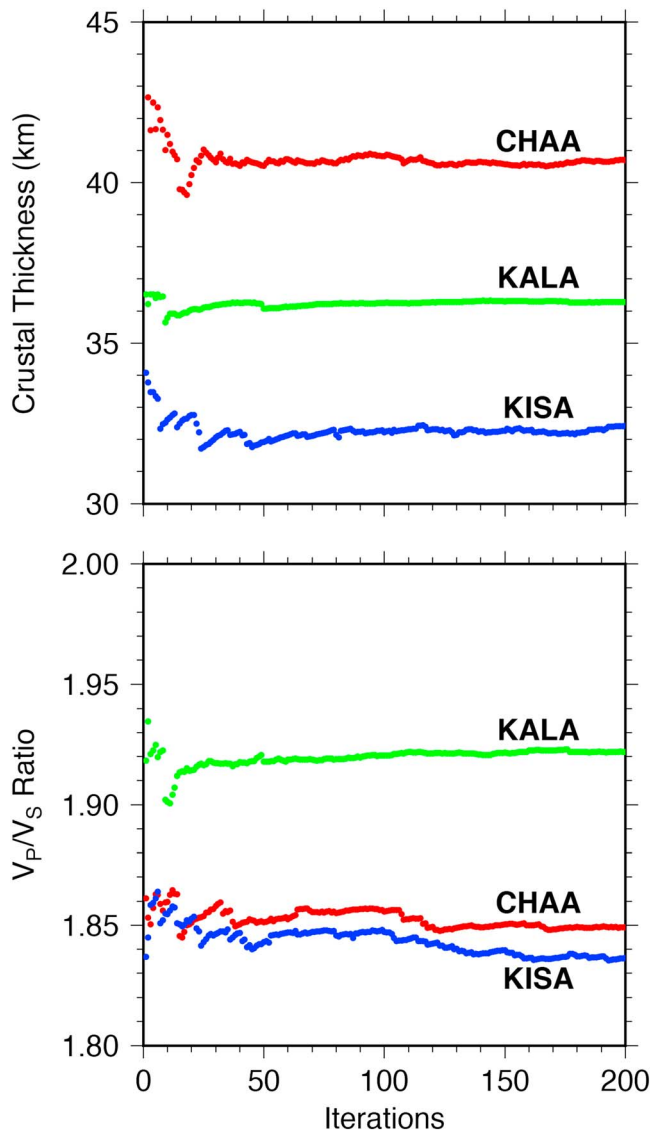
Figure 6. The convergence plots for (top) crustal thickness and (bottom) V_P/V_S ratio using bootstrap resampling. Convergence is observed for both characteristics at 200 iterations.

the receiver function will be incorporated into the stack. Each linear stack is weighted by the coherency of the instantaneous phases. To determine the coherency, the linear stack is multiplied by equation (6). The result is

$$g(t) = \frac{1}{N} \sum_{j=1}^{N} s_j(t) \left| \frac{1}{N} \sum_{k=1}^{N} e^{[i\phi_k(t)]} \right|^V, \qquad (7)$$

where V governs the effect the coherency values have on the H-κ stack. V remains 0 during a linear stack and has been taken as 2, an empirically derived constant, in this project for the phase weighted stack. Although the phase-weighted method aims to remove incoherent noise to make weaker signals more evident, it also has a tendency to remove later arrivals that have been misidentified as noise (Thurber et al., 2014). In addition, by manually selecting receiver functions that agree with calculated phase arrival times, the phase-weighted stacking becomes less important.

We perform a bootstrap analysis using both the linear and phase-weighted stacking, developing upon work by Efron and Tibshirani (1991) and Thompson et al. (2010), to test the robustness of our results. Before bootstrap analysis can be implemented the number of iterations required to achieve convergence must be determined. H-κ stacking is performed on a bootstrap sample which is randomly sampled, allowing for duplication, such that the number of receiver functions in the bootstrap sample is equal to that used in the linear H-κ stacking. The H and κ values are then calculated, and we calculate a moving average. This process is repeated until convergence in the H and κ values is observed in the moving average. Figure 6 shows convergence at 200 iterations in both the H and κ values. Therefore, 200 iterations of resampling were completed for each station. We use the variance in averages of each iteration to quantify the associated error.

Provided there is agreement between the linear and phase-weight stacking, defined as being where the results are within the range of error, and the magnitude of associated errors are acceptable we can interpret our results with a high level of confidence.

5. Results

Derived from the 40 events deemed high enough quality for analysis, 66 receiver functions were produced across the 11 seismometers (Table 1, Figures 7 and 8, and supporting information S1). We find that our results are reliable, with the exception of stations NINA and SUMA, which have relatively large errors associated with them (Table 1). The results for these two stations should therefore be treated with caution. We discuss our results as a range of acceptable results, as determined by the comprehensive error analysis. Crustal thickness and bulk V_P/V_S ratios have been presented independently for the region to make the results easier to follow.

5.1. Crustal Thickness

The 11 stations show variation in crustal thickness results from linear stacking from 31.6 km to 42 km with an average of 37.5 km. The second largest crustal thickness (41.1–42.1 km) is found at the northernmost station, SITA, near the dipping contact between Proterozoic Ubendian orogenic belt and the Archean craton. The majority of stations lie along the Ufipa Horst, also in the Ubendian belt, between the Tanganyika and Rukwa Rifts, where results for crustal thickness range from ~33 km to ~39 km.

Crustal thickness beneath stations within the fault-bounded sedimentary basins spans the range of values and shows a northward increase in crustal thinning, consistent with sedimentary thickness and age of faulting (e.g., Cohen et al., 1993; Morley, 1988). The smallest crustal thicknesses (32.4 km, 34.3 km, and

Table 1
Results From the H-κ Analysis

	Latitude (deg)	Longitude (deg)	NRF	H_{LIN_BS} (km)	H_{LIN_BS} error	κ_{LIN_BS}	κ_{LIN_BS} error	H_{PW_BS} (km)	H_{PW_BS} error	κ_{PW_BS}	κ_{PW_BS} error
CHAA	−7.59	31.27	10	**40.7**	6.7	**1.85**	0.12	**39.7**	6.2	**1.89**	0.09
KALA	−8.13	30.97	5	**36.3**	2.3	**1.92**	0.04	**36**	2.8	**1.93**	0.06
KASA	−8.44	31.15	4	**42**	1.1	**1.75**	0.03	**41.9**	1.1	**1.75**	0.03
KIPA	−7.43	30.59	9	**34.3**	8.7	**1.95**	0.17	**33**	11.8	**1.91**	0.17
KISA	−7.19	31.02	8	**32.4**	8	**1.84**	0.13	**35.9**	12.6	**1.77**	0.17
KOLA	−7.17	30.54	3	**31.6**	8.4	**1.97**	0.22	**38.8**	12.2	**1.93**	0.1
LAEA	−8.58	32.04	6	**39**	9.5	**1.87**	0.18	**39.6**	20.1	**1.77**	0.28
NAMA	−7.52	31.04	4	**37.3**	5.9	**1.95**	0.15	**35.3**	8.8	**1.96**	1.96
NINA*	−7.69	30.72	9	**39.6**	14.9	**1.86**	0.28	**35**	19.5	**1.84**	0.25
SITA	−6.62	31.14	5	**41.6**	0.5	**1.77**	0.02	**41.5**	0.7	**1.77**	0.03
SUMA*	−7.96	31.63	3	**37.9**	12.6	**1.93**	0.19	**34.9**	10.8	**1.95**	0.15

Note. NRF = number of receiver functions used in a stack. LIN = linear stack. PW = phase-weighted stack. BS = bootstrap results. Results at stations marked with an asterisk should be treated with caution due to large bootstrap errors. Entries in bold are the result values.
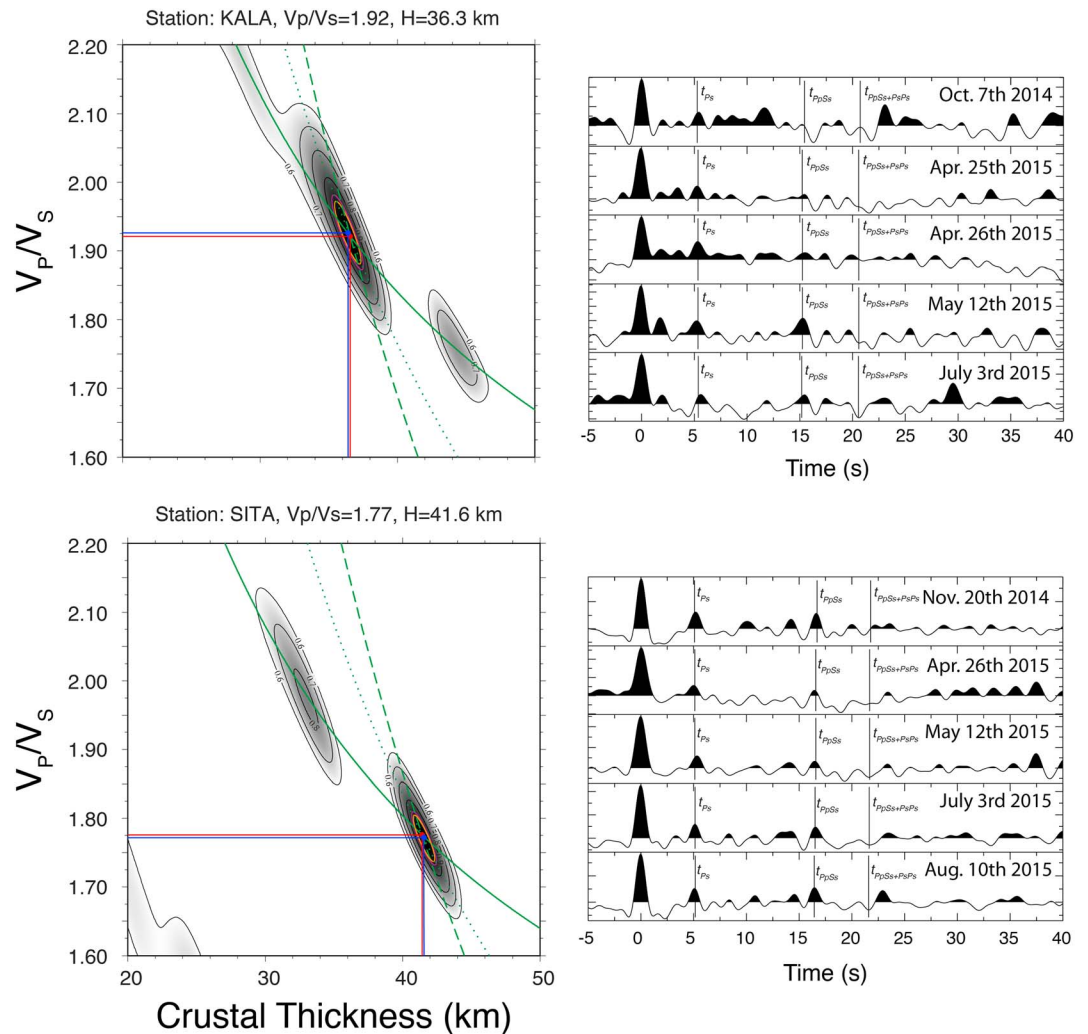

Figure 7. Examples of (left column) *H-κ* stacks and the (right column) receiver functions used to produce them showing the t_{Ps}, t_{PpPs}, and $t_{PpSs\ +\ PsSs}$ arrivals. Consistent agreement in the reverberation arrivals can be seen across all of the receiver functions used for analysis.
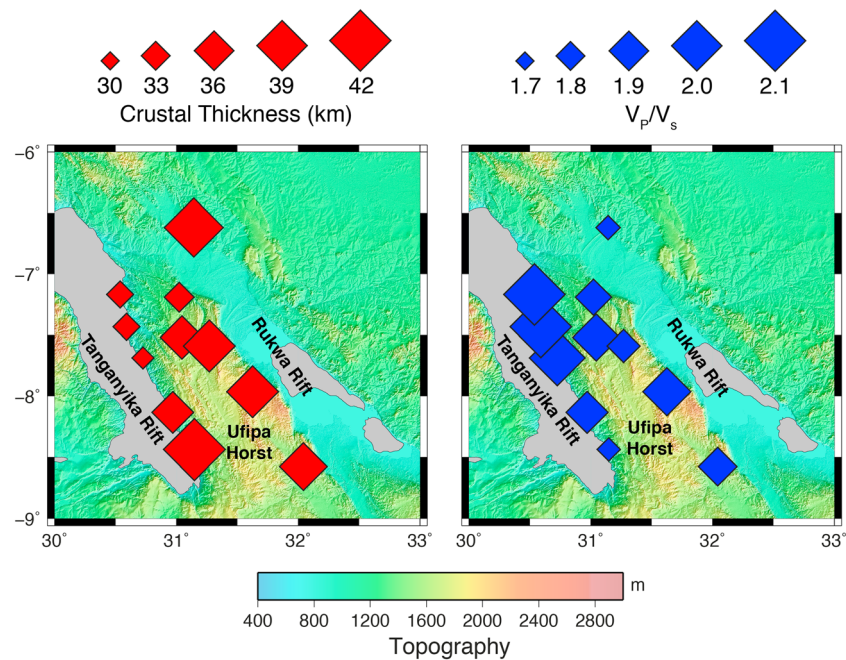
Figure 8. Variations in (left) crustal thickness and (right) V_P/V_S ratio taken from the linear stacking results (Table 1). Crustal thickness varies between 31.6 km and 42.0 km. Thinner crust can be seen flanked by thicker crust to the north and south. V_P/V_S ratios vary from 1.75 to 1.97 where high V_P/V_S ratios correspond to low crustal thicknesses.

31.6 km) are obtained at stations KISA, KIPA, and KOLA within the fault-bounded Moba basin segment, with the largest crustal thickness value of 42 km found at KASA at the southern end of the lake within the thinly sedimented Mpulungu basin, at the junction of the Southwestern and Western rift zones (Figures 1 and 8).

5.2. V_P/V_S Ratio

V_P/V_S ratios show large variations within the study area. The lowest V_P/V_S ratios are found near the Ubendian-Archean craton suture (1.77, SITA) and within the Bangweulu Block (1.75, KASA). The highest V_P/V_S values occur within the fault-bounded basins, at KOLA (1.97), and KIPA (1.95). These elevated V_P/V_S values may be caused by Moho complexity such as is observed in Northern California (Hayes & Furlong, 2007). KOLA and KIPA are near hydrothermal vent sites and elevated heat flow measurements (Figure 2). The average V_P/V_S ratio within the Ufipa Horst is 1.90, with some spatial variability.

5.3. Comparison to Previous Constraints

At the two sites (NAMA and LAEA) where we have obtained receiver functions at the same positions as earlier analyses by Tugume et al. (2012), we do not reproduce their crustal thickness (47.5 km and 46.7 km) or V_P/V_S (1.7 and 1.72) values. In general, we find crustal thicknesses vary far more from site to site, with stations in the Ubendian belt yielding lower crustal thickness and higher V_P/V_S than by Tugume et al. (2012). We attribute differences in results to the very narrow (43.5–48.5 km) window across which Tugume et al. (2012) restricted the grid search for crustal thickness and V_P/V_S ratio (1.48–1.98) during the H-κ stacking process. Consequently, the smaller crustal thicknesses of 37.3 and 39 km that we resolve would not have been possible solutions in their analysis.

6. Discussion

6.1. Crustal Thinning

Our crustal thickness results for KASA and SITA lie within the typical crustal ranges of Archean shields (Zandt & Ammon, 1995). The spatial variations in crustal thickness reveal fairly uniform thickness crust beneath the uplifted flanks of the Tanganyika and Rukwa Rift zones: 35–42 km which is similar to values found in Archaean-Pan-African crust in East Africa (Fishwick & Bastow, 2011; Tugume et al., 2012). The crust is much

thinner beneath the fault-bounded sedimentary basins. KISA (32.4 km) lies within the NW striking transfer fault zone linking the Rukwa border fault to the Tanganyika transfer faults, which continue beneath the lake. If an initial Proterozoic crustal thickness of 40 km is assumed, crustal thicknesses beneath the Marungu basin and within the accommodation zone between the Marungu and Mpulungu basins suggest a stretching factor of 1.23. The 25% decrease in crustal thickness from the flanks to the fault bounded Tanganyika basins reveals more stretching than originally estimated from balanced reconstructions of basement-involved faults imaged in seismic reflection profiles (10%; Morley, 1988), which only consider the brittle deformation within the crust, and from flexural modeling of basin and flank morphology (~15%; Ebinger et al., 1993), which were loosely constrained by assumed crustal thickness.

Crustal thicknesses in the Tanganyika Rift increase progressively southward. This along-rift change in crustal thickness is consistent with the southern Tanganyika Rift and northern Rukwa Rift overlapping in en echelon rift segments. Extension in the southern Tanganyika Rift is progressively transferred to the Rukwa Rift, and to the Mweru rift and Southwestern Branch (Figures 2 and 8). The crust between the overlapping rifts is also thinned (mean of 36.5 km) relative to the stable cratons, suggesting distributed strain occurs across the intervening Ufipa Horst.

Moho gradients have been shown to affect the results of H-κ stacking (Lombardi et al., 2008; Tomlinson et al., 2006). The crustal thickness results that we present here suggest a Moho that dips away from the rift (Figure 11), a pattern observed in the Eastern rift (Plasman et al., 2017). The majority of the earthquakes used in our study have a back azimuth in the northeast direction (Figure 3). They will be arriving, therefore, from the downdip direction of the Moho. Models of receiver functions by Lombardi et al. (2008) show that receiver functions with a back azimuth in the downdip direction will cause a slight overestimation in crustal thickness and a slight underestimate in V_P/V_S, whereas the affect is much stronger and opposite for receiver functions from the updip direction. The greatest difference in crustal thicknesses in our study are at KOLA and SITA, which are ~90 km apart (Figure 1). The Moho dip between these stations is ~5.6° NE. This dip would result in a maximum error in crustal thickness and V_P/V_S of ±0.5 km and ±0.02, respectively (Lombardi et al., 2008). We can therefore conclude that errors related to Moho gradients do not significantly affecting our results.

6.2. V_P/V_S Ratio

The largest crustal thicknesses obtained (42 km and 41.6 km), at KASA and SITA correspond with the lowest V_P/V_S values (1.75 and 1.77). Zandt and Ammon (1995) found Archean Shields to have V_P/V_S ratios of 1.78, attributing this to the abundance of quartz and plagioclase feldspar. These characteristics are a result of formation occurring prior to the onset of modern plate tectonics, when mantle temperatures were higher during the Archean (Durrheim & Mooney, 1991).

The average V_P/V_S ratio obtained in this study is 1.89, which is substantially higher than the Late Proterozoic crustal average of 1.73 (Guerri et al., 2015), and of V_P/V_S values in the Ugandan sector of the Western rift (Gummert et al., 2015). Excluding the results from stations on cratonic lithosphere, an average V_P/V_S ratio within the Ufipa Horst of 1.91 is found. Anorthosite and ultramafic bodies in the Ubendian belt locally may contribute to the regionally high V_P/V_S values (e.g., Lenoir et al., 1994). The ultramafic components and high plagioclase content of anorthosite leads to high V_P/V_S values of 1.9 (Christensen, 1996). The isolated bodies of anorthosite and ultramafic rocks are not sufficient to explain our high V_P/V_S values. It may be that the up to 7 km thick sedimentary strata, which typically have V_P/V_S ratios of 1.83–2.10 (Zhao et al., 2010), locally contribute to the high V_P/V_S ratio. A thick sedimentary layer will produce a converted PS phase from the base of the layer. The resolution of the receiver function method rarely is sufficient to distinguish between such converted phases and the direct P arrival (e.g., Cornwell et al., 2010). A significant sediment layer therefore results in a delayed direct P arrival (Cornwell et al., 2010; Langston, 2011; Yu et al., 2015), we do not observe this in any of our receiver functions and we conclude that sediments do not significantly affect our results. Therefore, a mafic component to the bulk composition of the crust (Figure 9), may be required to explain the elevated V_P/V_S.

The order of magnitude smaller volume of magma erupted in the Western rift has been attributed (1) to much smaller amounts of thinning, in the Western rift, with a lithosphere too thick for melting to occur (e.g., Ebinger et al., 1993; Pérez-Gussinyé et al., 2009) and (2) to the location of hot upwelling on the
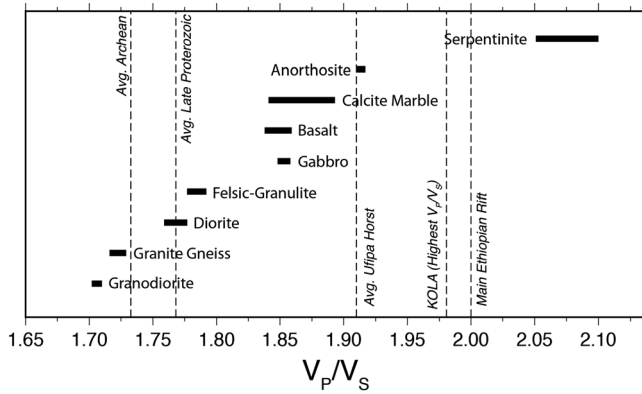
Figure 9. The range of V_P/V_S values for typical crustal lithologies (Christensen, 1996) with significant V_P/V_S values obtained from this project. The Main Ethiopian Rift and average global values have been taken from Stuart et al. (2006) and Guerri et al. (2015), respectively. The V_P/V_S values from Christensen (1996) were obtained at constant pressure-temperature conditions, it is important to note that Guerri et al. (2015) has revealed greater variation when a full range of crustal pressure-temperature conditions are used.

eastern side of the Tanzania craton (e.g., Fishwick, 2010; Weerarante et al., 2003). The lack of surface volcanism and absence of shallow earthquake swarms characterizing other African diking events, in addition to normal lithospheric seismic velocities led O'Donnell et al. (2014) to suggest that the Tanganyika rift is undergoing amagmatic extension.

The highest V_P/V_S ratios of 1.97 and 1.95 at KOLA and KIPA have been found at stations near hydrothermal vents and areas of elevated heat flow within the rift (Coussement et al., 1994; Ebinger et al., 1991; Lenoir et al., 1994). Fluid circulation along the deeply penetrating normal and oblique-slip fault systems could explain the hot springs and hydrothermal vents, but the heat flow values indicate elevated geotherms across the basin, considering the relative minor stretching that has occurred. An alternative mechanism to explain the high V_P/V_S, elevated geotherms, and deep seismicity is through the addition of magma to the base of the crust beneath some parts of the Marungu basin. If the mantle was stretched by the same amount as the crust, an originally 130 km thick lithosphere could be thinned to the liquidus, generating small melt fractions (e.g., Keen, 1985; Van Wijk et al., 2001), with or without the hotter temperatures of a mantle plume. V_P/V_S ratios larger than 1.94 are usually representative of fluid filled pores or fractures (Wang et al., 2009; Zandt & Ammon, 1995), or partially molten rocks supporting the hypothesis of fluids in the lower crust. With stretching values near the limit of magma production, one may expect patchy occurrences related to small variations in original lithospheric thickness, volatile content, and stretching.

Elevated V_P/V_S ratios have been interpreted as resulting from mafic intrusions at other rifts globally. Using receiver functions, Plasman et al. (2017) also find elevated V_P/V_S (1.85–1.97) and a gradational Moho in areas of magma intrusion imaged in tomography models (Roecker et al., 2017) from the Magadi-Natron-Manyara sector of the Eastern rift, which formed in Archaean lithosphere. Daly et al. (2008) performed a tomographic inversion to produce a 3-D P wave model of the Main Ethiopian Rift and identified high κ values (1.81–1.84) along the rift axis at a consistent depth which were interpreted as cooled mafic intrusions. Furthermore, the elevated V_P/V_S values, in addition to supplemental geophysical evidence, implied significant dyking from midcrustal depths to the surface. Higher κ values (1.85–1.93) across the Main Ethiopian Rift were interpreted
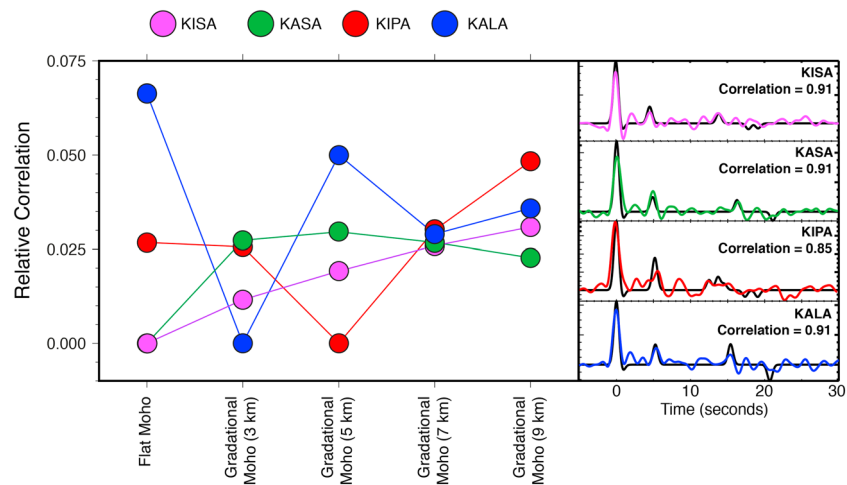

Figure 10. (left) Correlation results between observed receiver functions and modeled receiver functions, calculated with a maximum frequency of 1 Hz. High relative correlation indicates the best match between observed and modeled receiver functions. Results show that stations within the Ufipa Horst (KISA, KASA, and KIPA) show evidence for a gradational Moho, whereas stations that lie toward the edge of the rift show evidence for a less altered, flatter Moho (KALA). (right) Observed receiver function stacks (colored) compared to the synthetic receiver function (black) which produced the highest correlation.
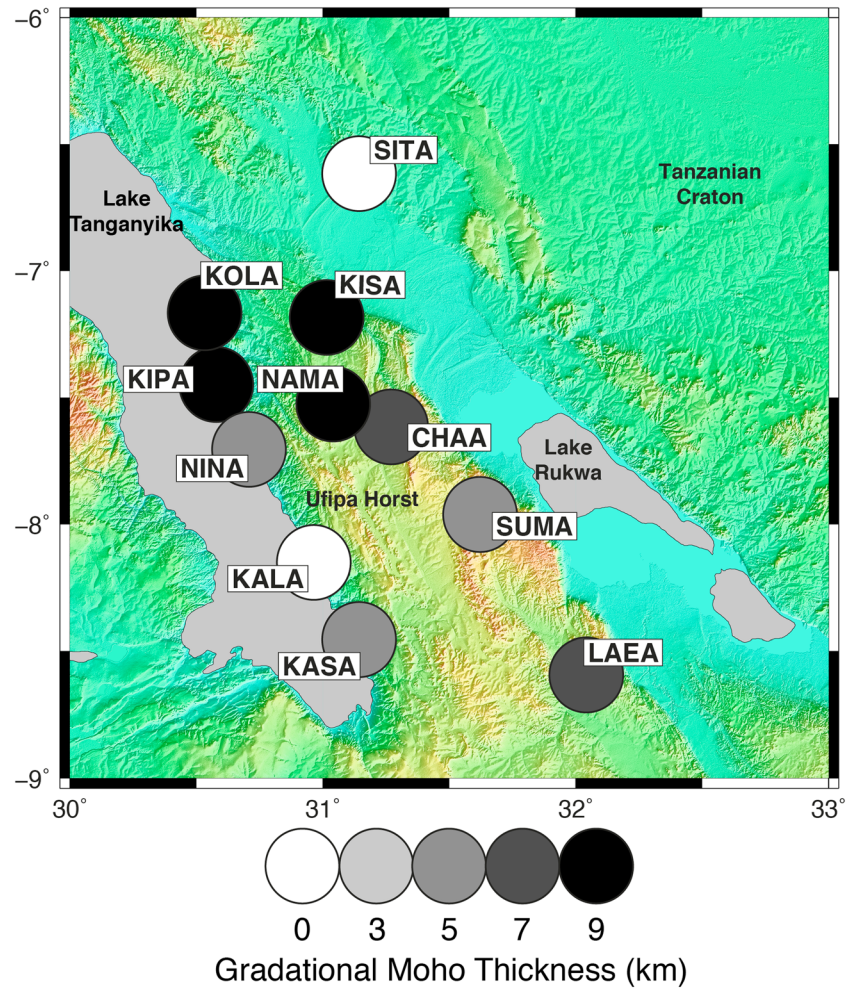
Figure 11. Results of the forward modeling for each station. Displayed results are the best fit model for receiver functions calculated with a maximum frequency of 1 Hz. We see an increase in the width of the gradational Moho beneath the Ufipa Horst.

as frozen gabbroic sills which could potentially contain some partial melt (Cornwell et al., 2010). Therefore, it is likely that the elevated V_P/V_S values obtained by our study are at least partly a result of mafic addition to the crust, the source of which could be magmatic intrusions into the lower crust.

If magmatic intrusions have affected the lower crust in the region, they would be expected to alter the nature of the Moho to become more gradational (e.g., Thybo & Artemieva, 2013, and references therein). To investigate this, we performed forward modeling of receiver functions for a range of crustal models with an increasingly gradational velocity increase at the Moho (Helffrich, 2006; Langston, 1979; Ligorria & Ammon, 1999; Randall, 1989). We tested a sharp Moho, and gradations of 3 km, 5 km, 7 km, and 9 km. We then calculated the correlation over the t_1 and t_2 arrivals of each model with the calculated receiver functions at each station, selecting the model with highest correlation as the best fit (Figure 10). Each gradation has a P wave velocity that increases from 6.6 km s^{-1} to 8 km s^{-1}, with S wave velocities increasing relative to the calculated V_P/V_S ratio. In addition, we repeated the modeling with receiver functions calculated with maximum frequencies of 1 Hz, 1.5 Hz, and 2 Hz in order to test the models with increasing vertical resolution. Attenuation within the crust is not considered in the modeling of receiver functions, and therefore, care must be taken when comparing the amplitudes of the t_1 and t_2 phases to the receiver function data, which will be affected by attenuation. We found that results were consistent across the different frequency ranges.

The results of the forward modeling suggest that the width of Moho gradation generally increases within the Ufipa Horst (Figure 11). In particular, we see Moho gradations of 9 km at stations KOLA, KISA, KIPA, and NAMA. These stations also display some of the highest V_P/V_S ratios (Figure 8). If we assume that prior to any
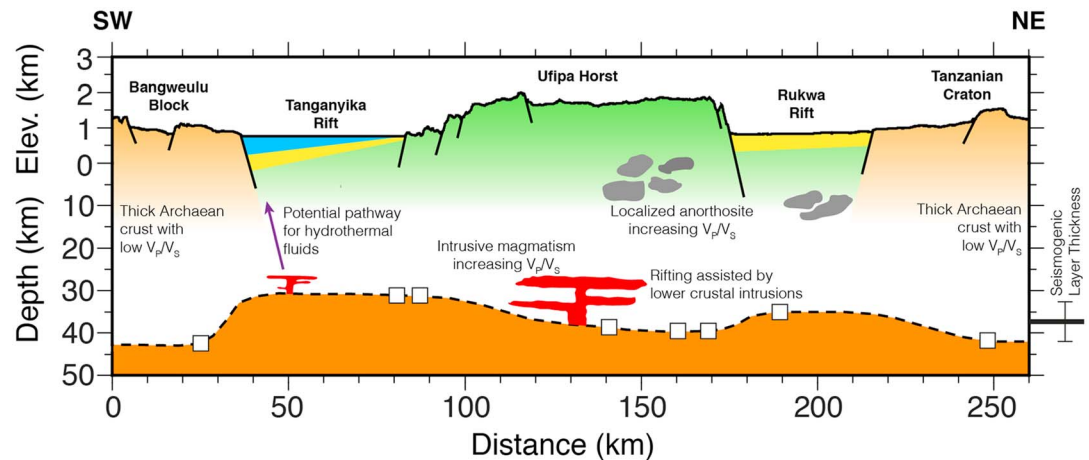
Figure 12. A summary of the geological interpretations from this project. Vertical exaggeration of 10:1 above sea level and 1.2:1 below sea level. White squares indicate crustal thickness measurements. Seismogenic layer thickness of 37 ± 5 km from Yang and Chen (2010). The size of magmatic bodies has been exaggerated. Lower crustal intrusions in the form of dykes, sills, or ponded magma are assisting SW-NE oriented rifting within the Ubendian Mobile belt. This results in increased V_P/V_S ratios within the belt. Isolated anomalously high V_P/V_S can be attributed to localized anorthosite or underplated mantle which can feed magma chambers within the crust. These provide a setting for the generation of hydrothermal fluids. High angle normal faulting provides a potential pathway for the fluids to vent sites at the surface. Thick, lithospherically strong Archean cratons flank the rift and show no magmatic modification due to rifting.

magmatic modification, the Moho was nongradational, the combination of elevated V_P/V_S values and gradational Moho within the Ufipa Horst provides evidence that deep magmatic activity is occurring beneath the southern Tanganyika Rift (Figure 11). Further, our study suggests that the absence of surface volcanism is a poor predictor of lower crustal magmatism during early stage rifting. This is especially important in young rifts, where there has potentially been insignificant time to evolve the widespread and focused magma plumbing systems required to develop focused surface volcanic centers.

The crustal thickness estimate of ~32 km may underestimate maximum stretching across the Marungu basin, owing to the station location on the monoclinal side of the asymmetric basin. It remains possible that some of the six teleseisms beneath the Southern Tanganyika rift with focal depths of 30 to 37 km occurred in the upper mantle. Specifically, the mb 6.5 2 October 2000 Marungu basin earthquake had a focal depth of 37 ± 5 km (Yang & Chen, 2010) (Figure 12). The lower depth limit places the earthquake at the Moho and could indicate active dike intrusion and underplating as a cause of the unusual seismicity. Further tests of these interpretations await better seismic network coverage of the lake and its western margins.

7. Conclusions

We analyzed receiver functions from 11 stations at the Tanganyika Rift of the EAR to test whether magma intrusion has modified the crust during rifting, without geomorphic expression of volcanism. Crustal thickness varies from 31.6 km to 42.0 km with an average of 37.5 km. Crustal thicknesses on/near the relatively unextended Tanzanian craton and Bangweulu Block are 42.0 km and 41.6 km, respectively. This contrasts in the Tanganyika Rift where crustal thicknesses are 31.6 to 39.0 km from north to south. Crust in the Ufipa Horst between the Tanganyika Rift and the Rukwa Rift is thinned relative to the crust along the rift flanks. Assuming a conservative value of 40 km for prerift crustal thickness (e.g., Last et al., 1997), our new crustal thickness estimates in the Marungu basin are consistent with a stretching factor of up to 1.25. Crustal stretching decreases southward between the Marungu and Mpulungu basins, consistent with decreasing sedimentary fill and inferred basin age (Cohen et al., 1993), and with progressive southward transfer of extension from the Tanganyika Rift to the Rukwa Rift.

The lowest V_P/V_S ratios of 1.75 and 1.77 are found near the Ubendian-Archaean suture zone, and in the Bangweulu Block, respectively, consistent with expected felsic composition. Elevated V_P/V_S elsewhere in the Ubendian belt (1.84–1.97) are consistent with presence of mafic and ultramafic composition. The high V_P/V_S may indicate crustal modification by magmatic intrusion, a hypothesis supported by high heat flow,

the presence of hydrothermal vents, and earthquakes at the crust-mantle boundary. Additionally, Proterozoic anorthosites and ultramafic bodies may locally contribute to elevated V_P/V_S. Our results provide the first evidence the onset of magmatic intrusion in the southern Tanganyika Rift, and a potential explanation for the frequent lower crustal earthquakes in this actively deforming zone.

References

Accardo, N., Gaherty, J. B., Shillington, D. J., Ebinger, C. J., Nyblade, A. A., Mbogoni, G. J., … Chindandali, P. R. N. (2017). Surface-wave imaging of the weakly-extended Malawi Rift from ambient-noise and teleseismic Rayleigh waves. *Geophysical Journal International*, *209*(3), 1892–1905. https://doi.org/10.1093/gji/ggx133

Bellucci, J. J., McDonough, W. F., & Rudnick, R. L. (2011). Thermal history and origin of the Tanzanian Craton from Pb isotope thermochronology of feldspars from lower crustal xenoliths. *Earth and Planetary Science Letters*, *301*(3-4), 493–501. https://doi.org/10.1016/j.epsl.2010.11.031

Bialas, R. W., Buck, W. R., & Qin, R. (2010). How much magma is required to rift a continent? *Earth and Planetary Science Letters*, *292*(1-2), 68–78. https://doi.org/10.1016/j.epsl.2010.01.021

Buck, W. R. (2004). Consequences of asthenospheric variability on continental rifting. *Rheology and deformation of the lithosphere at continental margins*, *62*, 1–30.

Chakrabarti, R., Basu, A. R., Santo, A. P., Tedesco, D., & Vaselli, O. (2009). Isotopic and geochemical evidence for a heterogeneous mantle plume origin of the Virunga volcanics, Western rift, East African Rift system. *Chemical Geology*, *259*(3-4), 273–289. https://doi.org/10.1016/j.chemgeo.2008.11.010

Christensen, N. I. (1996). Poisson's ratio and crustal seismology. *Journal of Geophysical Research*, *10*, 3139–3156.

Christensen, N. I., & Mooney, W. D. (1995). Seismic velocity structure and composition of the continental crust: A global view. *Journal of Geophysical Research*, *100*(B6), 9761–9788. https://doi.org/10.1029/95JB00259

Cohen, A. S., Soreghan, M. J., & Scholz, C. A. (1993). Estimating the age of formation of lakes: An example from Lake Tanganyika, East African Rift system. *Geology*, *21*(6), 511–514. https://doi.org/10.1130/0091-7613(1993)021%3C0511:ETAOFO%3E2.3.CO;2

Cornwell, D. G., Maguire, K. H., England, R. W., & Stuart, G. W. (2010). Imaging detailed crustal structure and magmatic intrusion across the Ethiopian Rift using a dense linear broadband array. *Geochemistry, Geophysics, Geosystems*, *11*, Q0AB03. https://doi.org/10.1029/2009GC002637

Coussement, C., Gente, P., Rolet, J., Tiercelin, J. J., Wafula, M., & Buku, S. (1994). The North Tanganyika hydrothermal fields, East African Rift system: Their tectonic control and relationship to volcanism and rift segmentation. *Tectonophysics*, *237*(3-4), 155–173. https://doi.org/10.1016/0040-1951(94)90252-6

Craig, T. J., Jackson, J. A., Priestley, K., & McKenzie, D. (2011). Earthquake distribution patterns in Africa: Their relationship to variations in lithospheric and geological structure, and their rheological implications. *Geophysical Journal International*, *185*(1), 403–434. https://doi.org/10.1111/j.1365-246X.2011.04950.x

Daly, E., Keir, D., Ebinger, C. J., Stuart, G. W., Bastow, I. D., & Ayele, A. (2008). Crustal tomographic imaging of a transitional continental rift: The Ethiopian rift. *Geophysical Journal International*, *172*(3), 1033–1048. https://doi.org/10.1111/j.1365-246X.2007.03682.x

Debayle, E., Lévêque, J. J., & Cara, M. (2001). Seismic evidence for a deeply rooted low-velocity anomaly in the upper mantle beneath the northeastern Afro/Arabian continent. *Earth and Planetary Science Letters*, *193*(3-4), 423–436. https://doi.org/10.1016/S0012-821X(01)00509-X

Durrheim, R., & Mooney, W. (1991). Archean and Proterozoic crustal evolution: Evidence from crustal seismology. *Geology*, *19*(6), 606. https://doi.org/10.1130/0091-7613(1991)019%3C0606:AAPCEE%3E2.3.CO;2

Eaton, D. W., Dineva, S., & Mereu, R. (2006). Crustal thickness and V_P/V_S variations in the Grenville orogen (Ontario, Canada) from analysis of teleseismic receiver functions. *Tectonophysics*, *420*(1-2), 223–238. https://doi.org/10.1016/j.tecto.2006.01.023

Ebinger, C. J. (1989). Tectonic development of the western branch of the East African rift system. *Geological Society of America Bulletin*, *101*(7), 885–903. https://doi.org/10.1130/0016-7606(1989)101%3C0885:TDOTWB%3E2.3.CO;2

Ebinger, C. J., & Sleep, N. H. (1998). Cenozoic magmatism throughout east Africa resulting from impact of a single plume. *Nature*, *395*(6704), 788–791. https://doi.org/10.1038/27417

Ebinger, C., Karner, G., & Weissel, J. (1991). The strength of extended continental lithosphere: Constraints from the Western rift system. *Tectonics*, *10*(6), 1239–1256. https://doi.org/10.1029/91TC00579

Ebinger, C. J., Deino, A. L., Tesha, A. L., Becker, T., & Ring, U. (1993). Tectonic controls on rift basin morphology: Evolution of the Northern Malawi (Nyasa) Rift. *Journal of Geophysical Research*, *98*(B10), 17,821–17,836. https://doi.org/10.1029/93JB01392

Ebinger, C. J., van Wijk, J., & Keir, D. (2013). The time scales of continental rifting: Implications for global processes. *Geological Society of America Special Papers*, *500*, 371–396. https://doi.org/10.1130/2013.2500

Efron, B., & Tibshirani, R. (1991). Statistical data analysis in the computer age. *Science*, *253*(5018), 390–395. https://doi.org/10.1126/science.253.5018.390

Fishwick, S. (2010). Surface wave tomography: Imaging of the lithosphere–asthenosphere boundary beneath central and southern Africa? *Lithos*, *120*(1-2), 63–73. https://doi.org/10.1016/j.lithos.2010.05.011

Fishwick, S., & Bastow, I. D. (2011). Towards a better understanding of African topography: A review of passive-source seismic studies of the African crust and upper mantle. *Geological Society, London, Special Publications*, *357*(1), 343–371. https://doi.org/10.1144/SP357.19

Foster, A. N., & Jackson, J. A. (1998). Source parameters of large African earthquakes: Implications for crustal rheology and regional kinematics. *Geophysical Journal International*, *134*(2), 422–448. https://doi.org/10.1046/j.1365-246x.1998.00568.x

Gallacher, R. J., & Bastow, I. D. (2012). The development of magmatism along the Cameroon Volcanic Line: Evidence from teleseismic receiver functions. *Tectonics*, *31*, TC3018. https://doi.org/10.1029/2011TC003028

Guerri, M., Cammarano, F., & Connolly, J. A. D. (2015). Effects of chemical composition, water and temperature on physical properties of continental crust. *Geochemistry, Geophysics, Geosystems*, *16*, 2431–2449. https://doi.org/10.1002/2015GC005819

Gummert, M., Lindenfeld, M., Wölbern, I., Rümpker, G., Celestin, K., & Batte, A. (2015). Crustal structure and high-resolution Moho topography across the Rwenzori region (Albertine rift) from P-receiver functions. *Geological Society, London, Special Publications*, *420*.

Halldórsson, S. A., Hilton, D. R., Scarsi, P., Abebe, T., & Hopp, J. (2014). A common mantle plume source beneath the entire East African Rift System revealed by coupled helium-neon systematics. *Geophysical Research Letters*, *41*, 2304–2311. https://doi.org/10.1002/2014GL059424

Hammond, J. O. S., & Kendall, J. M. (2016). Constraints on melt distribution from seismology: A case study in Ethiopia. *Geological Society, London, Special Publications*, *420*(1), 127–147. https://doi.org/10.1144/SP420.14

Hansen, S. E., & Nyblade, A. A. (2013). The deep seismic structure of the Ethiopia/Afar hotspot and the African superplume. *Geophysical Journal International*, 116.

Hayes, G. P., & Furlong, K. P. (2007). Abrupt changes in crustal structure beneath the Coast Ranges of northern California-developing new techniques in receiver function analysis. *Geophysical Journal International*, 170(1), 313–336. https://doi.org/10.1111/j.1365-246X.2007.03401.x

Helffrich, G. (2006). Extended-time multitaper frequency domain cross-correlation receiver-function estimation. *Bulletin of the Seismological Society of America*, 96(1), 344–347. https://doi.org/10.1785/0120050098

Kampunzu, A. B., Kramers, J. D., & Makutu, M. N. (1998). Rb-Sr whole rock ages of the lueshe, Kirumba and Numbi igneous complexes (Kivu, Democratic Republic of Congo) and the break-up of the Rodinia supercontinent. *Journal of the African Earth Sciences*, 26(1), 29–36. https://doi.org/10.1016/S0899-5362(97)00134-6

Keen, C. E. (1985). The dynamics of rifting: Deformation of the lithosphere by active and passive driving forces. *Geophysical Journal International*, 80(1), 95–120. https://doi.org/10.1111/j.1365-246X.1985.tb05080.x

Koptev, A., Calais, E., Burov, E., Leroy, S., & Gerya, T. (2015). Dual continental rift systems generated by plume-lithosphere interaction. *Nature Geoscience*, 8(5), 388–392. https://doi.org/10.1038/ngeo2401

Langston, C. A. (1979). Structure under Mount Rainier, Washington, inferred from teleseismic body waves. *Journal of Geophysical Research*, 84(B9), 4749–4762. https://doi.org/10.1029/JB084iB09p04749

Langston, C. A. (2011). Wave-field continuation and decomposition for passive seismic imaging under deep unconsolidated sediments. *Bulletin of the Seismological Society of America*, 101(5), 2176–2190. https://doi.org/10.1785/0120100299

Last, R. J., Nyblade, A. A., Langston, C. A., & Owens, T. J. (1997). Crustal structure of the East African Plateau from receiver functions and Rayleigh wave phase velocities. *Journal of Geophysical Research*, 102(B11), 24,469–24,483.

Lenoir, J. L., Liegeois, J.-P., Theunissen, K., & Klerkx, J. (1994). The Palaeoproterozoic Ubendian shear belt in Tanzania: Geochronology and structure. *Journal of the African Earth Sciences*, 19(3), 169–184. https://doi.org/10.1016/0899-5362(94)90059-0

Ligorria, J. P., & Ammon, C. J. (1999). Iterative deconvolution and receiver-function estimation. *Bulletin of the Seismological Society of America*, 89(5), 1395–1400.

Lombardi, D., Braunmiller, J., Kissling, E., & Giardini, D. (2008). Moho depth and Poisson's ratio in the Western-Central Alps from receiver functions. *Geophysical Journal International*, 173(1), 249–264. https://doi.org/10.1111/j.1365-246X.2007.03706.x

McConnell, R. B. (1950). *Outline of the geology of Ufipa and Ubende*. Tanganyika: Bulletin of the Geological Survey.

Morley, C. K. (1988). Variable extension in Lake Tanganyika. *Tectonics*, 7(4), 785–801. https://doi.org/10.1029/TC007i004p00785

Morley, C. K., Cunningham, S. M., Harper, R. M., & Wescott, W. A. (1992). Geology and geophysics of the Rukwa Rift, East Africa. *Tectonics*, 11(1), 69–81. https://doi.org/10.1029/91TC02102

Mulibo, G. D., & Nyblade, A. A. (2013). Mantle transition zone thinning beneath eastern Africa: Evidence for a whole-mantle superplume structure. *Geophysical Research Letters*, 40, 3562–3566. https://doi.org/10.1002/grl.50694

Nyblade, A. A., Pollack, H. N., Jones, D. L., Podmore, F., & Mushayandebvu, M. (1990). Terrestrial heat flow in east and southern Africa. *Journal of Geophysical Research*, 95(B11), 17,371–17,384. https://doi.org/10.1029/JB095iB11p17371

O'Donnell, J. P., Nyblade, A., Mulibo, G. D., & Tugume, F. (2014). The uppermost mantle shear wave velocity structure of eastern Africa from Rayleigh wave tomography: Constraints on rift evolution. *Geophysical Journal International*, 194(2), 961–978.

O'Donnell, J. P., Selway, K., Nyblade, A. A., Brazier, R. A., El Tahir, N., & Durrheim, R. J. (2015). Thick lithosphere, deep crustal earthquakes and no melt: A triple challenge to understanding extension in the western branch of the East African Rift. *Geophysical Journal International*, 204(2), 985–998.

Park, J., & Levin, V. (2000). Receiver functions from multiple-taper spectral correlation estimates. *Bulletin of the Seismological Society of America*, 90(6), 1507–1520. https://doi.org/10.1785/0119990122

Pérez-Gussinyé, M., Metois, M., Fernández, M., Vergés, J., Fullea, J., & Lowry, A. R. (2009). Effective elastic thickness of Africa and its relationship to other proxies for lithospheric structure and surface tectonics. *Earth and Planetary Science Letters*, 287(1-2), 152–167. https://doi.org/10.1016/j.epsl.2009.08.004

Phinney, R. A. (1964). Structure of the Earth's crust from spectral behavior of long-period body waves. *Journal of Geophysical Research*, 69(14), 2997–3017. https://doi.org/10.1029/JZ069i014p02997

Plasman, M., Tiberi, C., Ebinger, C., Gautier, S., Albaric, J., Peyrat, S., … Gama, R. (2017). Lithospheric low-velocity zones associated with a magmatic segment of the Tanzanian Rift, East Africa. *Geophysical Journal International*, 210(1), 465–481. https://doi.org/10.1093/gji/ggx177

Randall, G. E. (1989). Efficient calculation of differential seismograms for lithospheric receiver functions. *Geophysical Journal International*, 99(3), 469–481. https://doi.org/10.1111/j.1365-246X.1989.tb02033.x

Roberts, E. M., O'Connor, P. M., Stevens, N. J., Gottfried, M. D., Jinnah, Z. A., Ngasala, S., … Armstrong, R. A. (2010). Sedimentology and depositional environments of the Red Sandstone Group, Rukwa Rift Basin, southwestern Tanzania: New insight into Cretaceous and Paleogene terrestrial ecosystems and tectonics in sub-equatorial Africa. *Journal of the African Earth Sciences*, 57(3), 179–212. https://doi.org/10.1016/j.jafrearsci.2009.09.002

Roberts, E. M., Stevens, N. J., O'Connor, P. M., Dirks, P. H. G. M., Gottfried, M. D., Clyde, W. C., … Hemming, S. (2012). Initiation of the western branch of the East African Rift coeval with the eastern branch. *Nature Geoscience*, 5(4), 284–294.

Roecker, S., Ebinger, C., Tiberi, C., Mulibo, G., Ferdinand-Wambura, R., Mtelela, K., … Peyrat, S. (2017). Subsurface images of the eastern rift, Africa, from the joint inversion of body waves, surface waves and gravity: Investigating the role of fluids in early-stage continental rifting. *Geophysical Journal International*, 210(2), 931–950. https://doi.org/10.1093/gji/ggx220

Rosendahl, B. R. (1987). Architecture of continental rifts with special reference to East Africa. *Annual Review of Earth and Planetary Sciences*, 15(1), 445–503. https://doi.org/10.1146/annurev.ea.15.050187.002305

Rosendahl, B. R., Reynolds, D. J., Lorber, P. M., Burgess, C. F., McGill, J., Scott, D., … Derksen, S. J. (1986). Structural expressions of rifting: Lessons from Lake Tanganyika, Africa. *Geological Society, London, Special Publications*, 25(1), 29–43. https://doi.org/10.1144/GSL.SP.1986.025.01.04

Schimmel, M., & Paulssen, H. (1997). Noise reduction and detection of weak, coherent signals through phase-weighted stacks. *Geophysical Journal International*, 130(2), 497–505. https://doi.org/10.1111/j.1365-246X.1997.tb05664.x

Scholz, C. A., Talbot, M. R., Brown, E. T., & Lyons, R. P. (2011). Lithostratigraphy, physical properties and organic matter variability in Lake Malawi drillcore sediments over the past 145,000 years. *Palaeogeography, Palaeoclimatology, Palaeoecology*, 303(1-4), 38–50. https://doi.org/10.1016/j.palaeo.2010.10.028

Sembroni, A., Faccenna, C., Becker, T. W., Molin, P., & Bekele, A. (2016). Long-term, deep-mantle support of the Ethiopia-Yemen Plateau. *Tectonics*, 35(2), 469–488. https://doi.org/10.1002/2015TC004000

Stamps, D. S., Iaffaldano, G., & Calais, E. (2015). Role of mantle flow in Nubia-Somalia plate divergence. *Geophysical Research Letters*, *42*(2), 290–296. https://doi.org/10.1002/2014GL062515

Stuart, G. W., Bastow, I. D., & Ebinger, C. J. (2006). Crustal structure of the northern Main Ethiopian Rift from receiver function studies. *Geological Society*, *259*(1), 253–267. https://doi.org/10.1144/GSL.SP.2006.259.01.20

Tedla, G. E., van der Meijde, M., Nyblade, A. A., & van der Meer, F. D. (2011). A crustal thickness map of Africa derived from a global gravity field model using Euler deconvolution. *Geophysical Journal International*, *187*(1), 1–9. https://doi.org/10.1111/j.1365-246X.2011.05140.x

Thompson, D., Bastow, I., Helffrich, G., Kendall, J.-M., Wookey, J., Snyder, D., & Eaton, D. (2010). Precambrian crustal evolution: Seismic constraints from the Canadian shield. *Earth and Planetary Science Letters*, *297*(3-4), 655–666. https://doi.org/10.1016/j.epsl.2010.07.021

Thomson, D. J. (1982). Spectrum estimation and harmonic analysis. *Proceedings of the IEEE*, *70*(9), 1055–1096. https://doi.org/10.1109/PROC.1982.12433

Thurber, C., Zeng, X., Thomas, A., & Audet, P. (2014). Phase-weighted stacking applied to low-frequency earthquakes. *Bulletin of the Seismological Society of America*, *104*(5), 1–6.

Thybo, H., & Artemieva, I. M. (2013). Moho and magmatic underplating in continental lithosphere. *Tectonophysics*, *609*, 605–619. https://doi.org/10.1016/j.tecto.2013.05.032

Tiercelin, J. J., Thouin, C., Kalala, T., & Mondeguer, A. (1989). Discovery of sublacustrine hydrothermal activity and associated massive sulfides and hydrocarbons in the north Tanganyika trough. *East African Rift. Geology*, *17*(11), 1053–1056.

Tomlinson, J. P., Denton, P., Maguire, P. K. H., & Booth, D. C. (2006). Analysis of the crustal velocity structure of the British Isles using teleseismic receiver functions. *Geophysical Journal International*, *167*(1), 223–237. https://doi.org/10.1111/j.1365-246X.2006.03044.x

Tugume, F., Nyblade, A., & Julia, J. (2012). Moho depths and Poisson's ratios of Precambrian crust in East Africa: Evidence for similarities in Archean and Proterozoic Crustal Structure. *Earth and Planetary Science Letters*, *73-81*, 355–356.

Van Wijk, J. W., Huismans, R. S., Ter Voorde, M., & Cloetingh, S. A. P. L. (2001). Melt generation at volcanic continental margins: No need for a mantle plume. *Geophysical Research Letters*, *28*(20), 3995–3998. https://doi.org/10.1029/2000GL012848

Wang, Q., Ji, S., & Xu, Z. (2009). V_P/V_S anisotropy and implications for crustal composition identification and earthquake prediction. *Acta Geologica Sinica*, *83*(4), 801–815. https://doi.org/10.1111/j.1755-6724.2009.00103.x

Weerarante, D., Forsyth, D., Fischer, K., & Nyblade, A. (2003). Evidence for an upper mantle plume beneath the Tanzanian Craton from Rayleigh wave tomography. *Journal of Geophysical Research*, *108*(B9), 2427.https://doi.org/10.1029/2002JB002273

Yang, Z., & Chen, W. P. (2010). Earthquakes along the East African Rift System: A multiscale, system-wide perspective. *Journal of Geophysical Research*, *115*, B12309. https://doi.org/10.1029/2009JB006779

Yu, Y., Song, J., Liu, K. H., & Gao, S. S. (2015). Determining crustal structure beneath seismic stations overlying a low-velocity sedimentary layer using receiver functions. *Journal of Geophysical Research: Solid Earth*, *120*, 3208–3218. https://doi.org/10.1002/2014JB011610

Zandt, G., & Ammon, C. J. (1995). Continental crust composition constrained by measurements of crustal Poisson's ratio. *Nature*, *374*(6518), 152–154. https://doi.org/10.1038/374152a0

Zhao, M., Qiu, X., Xia, S., Xu, H., Wang, P., Wang, T. K., … Xia, K. (2010). Seismic structure in the northeastern South China Sea: *S*-wave velocity and V_P/V_S ratios derived from three-component OBS data. *Tectonophysics*, *480*(1-4), 183–197. https://doi.org/10.1016/j.tecto.2009.10.004

Zhu, L., & Kanamori, H. (2000). Moho depth variation in southern California from teleseismic receiver functions. *Journal of Geophysical Research*, *105*(B2), 2969–2980. https://doi.org/10.1029/1999JB900322